



# Scattering-based super-resolution optical fluctuation imaging

SHIMON YUDOVICH,<sup>1,2,3,9</sup>  GREGOR POSNJAK,<sup>4</sup>  LIOR SHANI,<sup>1,2,5</sup> ETI TEBLUM,<sup>2</sup> TIM LIEDL,<sup>4</sup> JÖRG ENDERLEIN,<sup>6,7,10</sup>  AND SHIMON WEISS<sup>1,2,8,11</sup> 

<sup>1</sup>*Department of Physics, Bar-Ilan University, Ramat-Gan 5290002, Israel*

<sup>2</sup>*Institute for Nanotechnology and Advanced Materials, Bar-Ilan University, Ramat-Gan 5290002, Israel*

<sup>3</sup>*Department of Molecular and Cell Biology, University of California, Berkeley, California 94720, USA*

<sup>4</sup>*Faculty of Physics and CeNS, Ludwig-Maximilian-University Munich, München, 80539 Bayern, Germany*

<sup>5</sup>*School of Physics and Astronomy, University of Minnesota, Minneapolis, MN 55455, USA*

<sup>6</sup>*Third Institute of Physics-Biophysics, Georg August University, 37077 Göttingen, Germany*

<sup>7</sup>*Cluster of Excellence “Multiscale Bioimaging: from Molecular Machines to Networks of Excitable Cells” (MBExC), Georg August University, Germany*

<sup>8</sup>*Departments of Chemistry and Biochemistry, Physiology, and California NanoSystems Institute, University of California Los Angeles, Los Angeles, CA 90095, USA*

<sup>9</sup>*shimon.yudovich@gmail.com*

<sup>10</sup>*jenderl@gwdg.de*

<sup>11</sup>*sweiss@chem.ucla.edu*

**Abstract:** Super-resolution optical imaging has become a prominent tool in life and material sciences, allowing one to decipher structures at increasingly greater spatial detail. Among the utilized techniques in this field, super-resolution optical fluctuation imaging (SOFI) has proved to be a valuable approach. A major advantage of SOFI is its less restrictive requirements for generating super-resolved images of neighboring nano-structures or molecules, as it only assumes that the detected fluctuating light from neighboring emitters is statistically uncorrelated, but not necessarily separated in time. While most optical super-resolution microscopies depend on signals obtained from fluorescence, they are limited by photobleaching and phototoxicity. An alternative source for optical signals can be acquired by detecting the light scattered from molecules or nanoparticles. However, the application of coherent scattering-based imaging modalities for super-resolution imaging has been considerably limited compared to fluorescence-based modalities. Here, we develop scattering-based super-resolution optical fluctuation imaging (sSOFI), where we utilize the rotation of anisotropic particles as a source of fluctuating optical signals. We discuss the differences in the application of SOFI algorithms for coherent and incoherent imaging modalities and utilize interference microscopy to demonstrate super-resolution imaging of rotating nanoparticle dimers. We present a theoretical analysis of the relevant model systems and discuss the possible effects of cusp artifacts and electrodynamic coupling between nearby nano-scatterers. Finally, we apply sSOFI as a label-free novelty filter that highlights regions with higher activity of biomolecules and demonstrates its use by imaging membrane protrusions of live cells. Overall, the development of optical super-resolution approaches for coherent scattering-based imaging modalities, as described here, could potentially allow for the investigation of biological processes at temporal resolutions and acquisition durations previously inaccessible in fluorescence-based imaging.

© 2025 Optica Publishing Group under the terms of the [Optica Open Access Publishing Agreement](#)

## 1. Introduction

Super-resolution optical microscopy has become an important tool in modern biological research, material science, and nanoscience. Advances in super-resolution imaging such as stimulated

emission depletion (STED) microscopy [1], photo-activated localization microscopy (PALM) [2], stochastic optical reconstruction microscopy (STORM) [3], or structured illumination microscopy (SIM) [4] and their derivatives reached optical resolutions of a few tens of nanometers, and more recently, even down to single nanometers [5]. This dramatic resolution enhancement has led to several significant new discoveries [6–8]. Most of the existing methods rely on fluorescence that, while guaranteeing high specificity and sensitivity, is associated with significant shortcomings, most notably - photobleaching, phototoxicity, and/or the requirement of non-native gene expression. An alternative to fluorescence-based imaging can be found in imaging modalities that utilize elastic scattering from molecules or particles. Such imaging modalities, such as dark-field microscopy [9], reflection interference contrast microscopy (RICM) [10], and interference scattering microscopy (iSCAT) [11–13], have been developed to allow for sensitive optical imaging without the need for fluorescence labeling.

In interference-based microscopes such as RICM and iSCAT, the sample is illuminated by incident light, and one records the interference between the scattered electric field and a fraction of the back-reflected incident light. The interference between the weak scattered light with the orders-of-magnitude stronger incident light leads to an amplification of the weak scattering signal by orders of magnitude (heterodyne gain); this amplified signal is linearly proportional to the scattered electric field amplitude and is thus proportional to the third power of the scatterer's size. This makes interference microscopy orders of magnitude more sensitive than dark-field imaging. The combination of single-particle sensitivity achieved by utilizing coherent illumination as commonly used in iSCAT, the possibility of label-free imaging, and the absence of photobleaching, gives interference microscopy enormous potential and enables temporally unlimited, highly sensitive label-free imaging [11]. Label-free scattering-based microscopy in its different forms has already proven to be relevant in the study of actin networks [14], microtubules in mitotic spindles [15] and surface assays [16], mitosis characterization [17], initiation and dynamics of liquid-liquid phase separation [18], mass quantification of cells [19] and single proteins [20], neuronal deformation due to action potentials [21], and many other applications in the realms of life and material sciences [22,23]. However, while such microscopy techniques allowed for ultra-sensitive detection of small scatterers, the achievements of interference-based super-resolution imaging have been limited compared to their fluorescence-based counterparts [24].

In this work, we investigate the application of super-resolution optical fluctuation imaging (SOFI) [25] for sub-diffraction scattering-based imaging, which we term sSOFI. SOFI, which relies on cumulant analysis of stochastic fluctuations of optical signals, is advantageous over localization-based approaches since it does not require neighboring nano-objects to emit light in a temporally separated manner. The basic working principle of SOFI can be described as follows: assuming each image is generated by  $N$  discrete emitters/scatterers at positions  $\mathbf{r}_j$  ( $1 \leq j \leq N$ ), the intensity at the camera plane  $F(\mathbf{r}, t)$ , which is proportional to the sum of each individual time-dependent (fluctuating) emitted/scattered intensity, can be expressed as

$$F(\mathbf{r}, t) = \sum_{j=1}^N U(\mathbf{r} - \mathbf{r}_j) \varepsilon_j s_j(t). \quad (1)$$

Here,  $U(\mathbf{r})$  is the point spread function (PSF) of the applied imaging modality,  $\varepsilon_j$  is the brightness factor corresponding to the  $j$ th emitter/scatterer, and  $s_j(t)$  is the normalized time-dependent intensity of the  $j$ th emitter/scatterer. The above assumption, that the formed image is composed from the addition of independent and non-correlated PSFs from different point particles, is not valid for dark-field imaging, as further discussed in section 3.1. In second-order SOFI, one calculates the second-order cumulant image  $C_2(\mathbf{r}, \tau)$ :

$$C_2(\mathbf{r}, \tau) = \langle F(\mathbf{r}, t) F(\mathbf{r}, t + \tau) \rangle - \langle F(\mathbf{r}, t) \rangle^2 = \sum_{j=1}^N U^2(\mathbf{r} - \mathbf{r}_j) \varepsilon_j^2 [\langle s_j(t) s_j(t + \tau) \rangle - \langle s_j(t) \rangle^2], \quad (2)$$

where the angular brackets denote averaging over time  $t$ , and  $\tau$  is a freely chosen correlation time. The last expression on the right-hand-side is the sum of second-order cumulants of the signal trajectories  $s_j(t)$ , assuming all cross-cumulant contributions between different emitters/scatterers are negligible. It is important to note that this assumption requires statistical independence of amplitude fluctuations between different emitters/scatterers. Then, Eq. (2) shows that the second-order SOFI image is formed with the square of the original PSF, resulting in a resolution enhancement by a square root of two compared to the pure intensity image. Extending this analysis to higher cumulant orders results in the following form for the  $n$ th-order cumulant image [25]:

$$C_n(\mathbf{r}, \tau_1, \dots, \tau_{n-1}) = \sum_{j=1}^N U^n(\mathbf{r} - \mathbf{r}_j) \varepsilon_j^n w_j(\tau_1, \dots, \tau_{n-1}), \quad (3)$$

where  $w_j(\tau_1, \dots, \tau_{n-1})$  is a weighting function related to moments up to the  $n$ th order, which depends on the specific stochastic process underlying the fluctuating signal. Thus, the size of the PSF for an  $n$ th-order SOFI image is reduced by a factor of  $n^{1/2}$  compared to the original intensity image. We note that similar to the PSF, the brightness factor  $\varepsilon_j$  of each emitter/scatterer is also raised to the power of  $n$ , which can be limiting when calculating high-order cumulants for heterogeneous samples. In such cases, the increasing dynamic range can be treated by calculating the balanced cumulants, as described in Ref. [26]. Furthermore, applying deconvolution (Fourier reweighting) [27,28] in conjunction with knowledge of the system's optical PSF can provide an additional enhancement of  $n^{1/2}$ , bringing the total theoretical resolution enhancement factor to  $n$ . The fluctuations necessary for the implementation of SOFI can originate from fluorescent proteins [29], organic dyes [30], quantum dots [25], or carbon nanodots [31]. Other types of optical fluctuations, such as those originating from diffusion [32], diffusion-controlled FRET [33], or stochastic speckle illumination [34], have also been exploited for SOFI. To date, SOFI has been implemented through a number of imaging platforms, including wide-field microscopy [35], total internal reflection fluorescence microscopy [29], multi-plane wide-field fluorescence microscopy [36], spinning-disk confocal microscopy [37], and light sheet microscopy [38]. In addition, dynamic speckle illumination has been used to extend SOFI to acousto-optic and photo-acoustic tomography [39]. The major advantages of SOFI include simplicity, low cost, compatibility with different imaging platforms, the availability of a wide variety of blinking probes, flexibility in imaging conditions, low excitation power ideally suited for imaging living cells, and a useful trade-off between spatial and temporal resolutions [40].

In this work, we show that SOFI analysis could be applied to scattering-based imaging modalities such as interference microscopies. However, it is incompatible with dark-field microscopies, as the formed image contains an additional cross-term component between two neighboring emitters that inherently fluctuates in a manner correlated with the two emitters. Next, we experimentally demonstrate this approach by performing interference imaging of gold nanorod (AuNRs) dimer structures formed by DNA origami. Such engineered nano-rulers with conjugated scattering objects at pre-defined positions provide a testbed for the development of scattering-based super-resolution imaging. Here, polarization-sensitive imaging of AuNRs undergoing rotational diffusion produces movies with fluctuating scattered fields, analogous to fluorescence blinking, which is an essential component for applying SOFI and localization-based super-resolution routines. Finally, since the weight of each pixel in a SOFI image is produced by the cumulant of the corresponding detected intensity trajectory, it is possible to apply sSOFI as a novelty filter that highlights dynamic processes in a label-free manner. We demonstrate this approach by interference imaging of membrane protrusions in live cells and show that sSOFI offers a convenient approach to analyze such movies and produce fluctuation-sensitive contrast.

## 2. Materials and methods

### 2.1. Gold nanorod monomers and dimers

Gold nanorods were synthesized according to a modified protocol from Gonzalez-Rubio et al. [41], as described in [Supplement 1](#). The AuNRs were functionalized by mixing the rods (OD = 16 in 0.1% SDS) in a 6:5 volume ratio with a mixture of thiolated T-30 and T-8 DNA strands (Eurofins, 100  $\mu$ M concentration; 1:9 volume ratio) and freezing them at -80 °C for 30 min [42]. Excess DNA strands were removed by five rounds of Amicon spin filtration (100 kDa) for 6 min at 5 k RCF and 25 °C prior to hybridization with the DNA origami structure.

The DNA origami structure used for the formation of the AuNR dimers was the rectangular Rothmund DNA origami structure (RRO), with eight biotinylated staple strands (Eurofins Genomic) for attachment to the BSA–biotin–streptavidin treated surface [43]. Dedicated binding strands for DNA-functionalized AuNRs and fluorophores were designed using the Picasso software package [43], with the binding strands' positions shown in Fig. S1. Oligo strands at two opposing corners of the rectangular structure, approximately 80 nm apart, were modified on their 3' ends with the sequence: 5'-TT CATATGAATTGCATGGTACC AAAAAAAAAAAAAAAAAAAAAAAAAAAAAAAAAA-3', where the first TT nucleotides are a spacer between the origami and the anchor strand, and the A-30 part is the particle binding sequence that hybridized with the T-30 strands on the AuNRs. The 20 nt part between the TT and the poly-A is a spacer that was hybridized by the addition of a complementary strand with the sequence: 5'-GGTACCATGCAATTCATATG-3'. In order to fluorescently label the DNA origami structures, oligo strands in four central positions of the structure were modified on their 3' ends with the sequence: 5'-TTCCTCTACCACCTACATCACA-3', which was then hybridized with the complementary strand modified with an ATTO 647N fluorophore on its 5' end (IDT). The folding mixture for forming the DNA origami structure, comprised of the single-stranded p7249 DNA scaffold (10 nM) and all staple strands (100 nM each) in buffer containing 10 mM Tris-HCl, 1 mM EDTA (pH adjusted to 8.0 with NaOH) and 12.5 mM MgCl<sub>2</sub>, was subject to thermal annealing in a thermal cycler (Techne), in which the reaction mixture was first heated to 80 °C for 5 min. Then, gradual cooling from 60 to 10 °C was applied, with a 1 °C decrease every 5 min. Excess DNA strands were removed by five rounds of Amicon spin filtration (100 kDa) for 15 min at 2 k RCF and 4 °C. The folded and purified DNA origami structures were then immobilized on glass coverslips precoated with BSA–biotin–streptavidin. For coating, coverslips were first cleaned by 5 min sonication in detergent solution (2% Hellmanex III; Hellma), double-distilled water, and acetone, then treated with 1 mg/ml BSA-biotin (Sigma-Aldrich) for 15 min and 0.5 mg/ml streptavidin (Thermo Fisher Scientific) for 5 min, both in 10 mM Tris-HCl, 100 mM NaCl and 0.05% (vol/vol) Tween 20 (pH 8). Multiple rounds of buffer exchange between and after coating steps were performed with the same buffer. DNA origami structures were diluted in 5 mM Tris-HCl, 10 mM MgCl<sub>2</sub>, 1 mM EDTA, and 0.05% (vol/vol) Tween 20 (pH 8) and introduced to the coverslip until sufficient surface covering was achieved. After multiple rounds of buffer exchange, AuNRs at a saturating binding concentration, diluted in the same buffer as the DNA origami, were introduced to the coverslip and allowed to bind to the DNA origami construct for 30 min, followed by extensive buffer exchanges.

Atomic force microscopy (AFM) measurements were conducted using a scanning probe microscope (Bio FastScan; Bruker, Karlsruhe, Germany). Images were obtained with a silicon probe (Fast Scan B, Bruker) in a soft tapping mode with a spring constant of 1.8 N/m. The cantilever was operated at a resonance frequency of approximately 450 kHz in an air environment. Image acquisition was performed in the retrace direction at a scanning speed of 1.6 Hz and 512 samples per line resolution. Image processing and artifact corrections were performed using an open-source software package (Gwyddion) [44].

## 2.2. Interference scattering microscopy

Interference scattering and fluorescence microscopy were performed on a home-built imaging system, as further described in [Supplement 1](#) and illustrated in Fig. S2. A 640 nm (LDH-D-C-640, PicoQuant) and a 470 nm (LDH D-C-470, PicoQuant) diode lasers were utilized for imaging the gold nanorods (section 3.2) and live cells (section 3.3), respectively. Both lasers were operated in a picosecond pulsed mode driven by the laser driver (PDL 800-D, PicoQuant), as it allowed for a shorter coherence length, which is advantageous for eliminating interference patterns created due to back-reflections in the optical path. In order to remove the speckle background for all imaging performed on AuNRs, average background images were produced by acquiring movies composed of 1000 frames captured while oscillating the stage parallel to the sample plane. Background correction was performed by dividing raw images with the averaged background images [45], and was applied to all imaging of AuNRs monomers and dimers. However, background correction was not applied to live cell imaging since the imaged region was too crowded to allow the acquisition of background resulting solely from the glass interface. Custom-written LabView (National Instruments) and MATLAB (MathWorks) software were used for all instrument control. Fluorescent beads (Spherotech) were sparsely dispersed on a coverslip and imaged in order to align the two cameras with respect to each other.

## 2.3. Colocalization with scanning electron microscopy

In order to compare, correlate, and benchmark sSOFI results, specific regions of interest were localized by scanning electron microscopy (SEM) after optical imaging. For this purpose, we fabricated indexed chrome micro-grids on top of glass coverslips (Fig. S3). Each grid comprised an array of 20  $\mu\text{m}$  x 20  $\mu\text{m}$  square cells fabricated via a standard photolithography process. Briefly, PMGI SF5 and AZ 1518 photoresist (MicroChemicals) were spin-coated on clean glass coverslips (Paul Marienfeld GmbH). The substrate was exposed to the grid pattern via a maskless lithography system (MLA 150, Heidelberg Instruments). Then, a 5 nm chrome layer was sputtered (Bestec GmbH) on the developed substrate. Finally, substrates were incubated in NMP for photoresist removal. Following optical imaging, the sample was allowed to dry overnight and then sputtered with an iridium layer. SEM imaging of AuNRs was performed on a high-resolution scanning electron microscope (Magellan 400 L, Thermo Fisher Scientific), with the optically imaged regions of interest located using the indexed micro-grid.

# 3. Results and discussion

## 3.1. Theoretical analysis of scattering-based SOFI

In order to study the application of SOFI algorithms to scattering-based imaging modalities and compare them with their use for conventional fluorescence-based imaging, we first produced and analyzed simulated movies of neighboring emitters/scatterers. Assuming two non-interacting fluorescent emitters or elastic scatterers that form an image in an incoherent or coherent superposition, respectively, each forming a PSF approximated by an Airy disk. In order to introduce a source temporal intensity fluctuation, we modeled each emitter/scatterer as an anisotropic emitter/scatterer rotationally diffusing in an isotropic manner, with the detected field from each particle calculated as the projection on an axis that is orthogonal to the sample plane. Rotational diffusion was simulated by implementing Monte Carlo simulations of a random walk on a sphere according to the algorithm described in Ref. [46]. All simulations and analyses were performed with MATLAB (MathWorks). Simulated frames were produced by assuming a coherent/incoherent superposition of the fields described by each PSF weighted by the corresponding time-varying amplitude. Incoherent images were produced by adding the intensities of either contributing PSF at each simulated pixel position. In reflection interference microscopies such as RICM and iSCAT, one captures the interference pattern between the

back-reflection of the incoming beam from the glass-water interface and the light scattered by the object of interest. In the case of two point scatterers, the (time-dependent) intensity distribution  $I(\mathbf{r}, t)$  of this image at the camera plane can be described by:

$$I(\mathbf{r}, t) = |E_{ref} + E_{scat,1}(\mathbf{r}, t) + E_{scat,2}(\mathbf{r}, t)|^2 \approx |E_{ref}|^2 + |E_{scat,1}(\mathbf{r}, t)|^2 + |E_{scat,2}(\mathbf{r}, t)|^2 + 2\text{Re}[E_{ref}E_{scat,1}^*(\mathbf{r}, t)] + 2\text{Re}[E_{ref}E_{scat,2}^*(\mathbf{r}, t)] + 2\text{Re}[E_{scat,1}(\mathbf{r}, t)E_{scat,2}^*(\mathbf{r}, t)], \quad (4)$$

where  $E_{ref}$  and  $E_{scat,1/2}$  are the electric field amplitude of the back-reflected (reference) and scattered light from the 1st and 2nd particle, respectively. An important precept in interference microscopies is that the intensity of the back-reflected light is orders of magnitudes stronger than that of the light scattered by sub-micron objects, so that the term proportional to  $|E_{scat,1/2}|^2$  can be neglected, while the mixed-term  $E_{ref}E_{scat,1/2}^*$  amplifies the scattered field considerably. In contrast, in the case of no reference field  $E_{ref} = 0$ , where only the scattered light is detected at the camera plane, as in dark-field imaging, the cross term between  $E_{scat,1}$  and  $E_{scat,2}$  becomes a significant contribution to the formed image.

Figure 1 shows SOFI auto-cumulant images ( $\tau = 0$ ) up to the 8th-order calculated from simulated movies of two such neighboring point sources, each undergoing stochastically independent rotational diffusion, assuming four different imaging modalities: (i) incoherent (fluorescence-like) imaging, (ii) dark-field imaging ( $E_{ref} = 0$ ), (iii) interference imaging with the reference field amplitude equal to the maximum scattered amplitude of each particle ( $E_{ref} = E_{scat}$ ), and (iv) interference imaging with the reference field is x100 greater than the maximum scattered amplitude of each particle ( $E_{ref} = 100E_{scat}$ ). The point sources are spatially fixed  $r_0/2$  apart from each other, where  $r_0$  is the Airy disk radius of the PSF each particle is assumed to produce in the incoherent imaging case. Several observations can be deduced from the results shown in Fig. 1. First, both dark-field imaging (Fig. 1(ii)), and interference-based imaging with a reference field that is not significantly more intense than the scattered fields (Fig. 1(iii)), contain cross-terms between the two scatterers in the image plane. Such cross-terms can be viewed as artificial objects introduced to the image plane, with fluctuation dynamics that are correlated with the fluctuation dynamics of both scatterers. Since the principal assumption in SOFI algorithms is that the time-varying amplitude of each contributing PSF is statistically independent from its neighboring scatterer, these two regimes are not suitable for the formation of super-resolved images with SOFI algorithms. We note that case (iv) represents the scenario in which contributions to the formed image from cross-terms between neighboring scatterers are negligible compared to their interference term with the reference field. Thus, increasing the amplitude of the reference field would result in an essentially identical image with a higher static background, which does not affect the SOFI image. In addition, while case (iv) demonstrates one model for interference imaging, other interference-based imaging methodologies [22] can be considered for the application of SOFI algorithms, as long as any cross-terms between individual neighboring scatterers are negligible in the formed image.

Another observation that can be made from Fig. 1 is that for both incoherent imaging (Fig. 1(i)) and interference imaging with a significantly strong reference field (Fig. 1(iv)), the SOFI images exhibit two super-resolved spots in some orders, but not others. In general, both of these modalities support the application of SOFI algorithms since their resulting images do not include significant cross-terms between the PSFs of neighboring emitters/scatterers. The origin of these artifacts in certain orders can be explained by calculating the cumulants from the expected intensity fluctuations. For the case of particles that undergo isotropic rotational diffusion and a polarization-sensitive imaging modality such as fluorescence anisotropy imaging or interference imaging with a strong reference field, one can model the stochastic emitted/scattered light intensity from each particle as a random walk on a sphere, with the time-dependent intensity

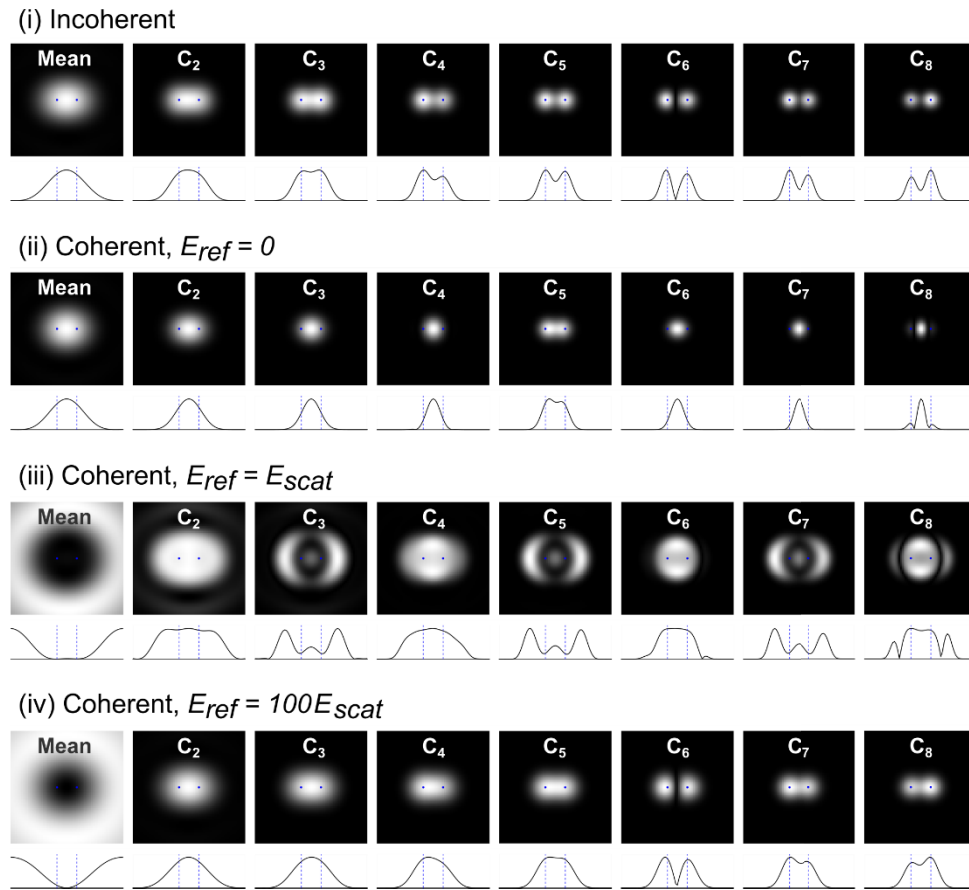


**Fig. 1.** SOFI analysis of simulated movies of fluctuating sources imaged by different modalities. Simulated movies of two neighboring rotationally diffusing emitters were produced by assuming each emitter forms an independent PSF described by an Airy function, with a time-varying amplitude fluctuating as a random walk on a sphere projected into one of its axes. For identical amplitude fluctuation trajectories, four different movies were formed, assuming frames were formed by (i) incoherent imaging, (ii) coherent darkfield imaging (no reference field), (iii) coherent interference imaging, where the reference field has the same amplitude as each emitter PSF's peak amplitude, and (iv) coherent interference imaging, where the amplitude of the reference field is 100 times greater than the peak amplitude of each emitter. For each movie, the mean intensity image and auto-cumulant images ( $\tau = 0$ ) up to the 8th-order are shown (top), together with the cross-section of the line passing through both emitters (bottom). Isotropic rotational diffusion was performed with a time step  $\Delta t = 0.01D_r$ , where  $D_r$  is the rotational diffusion coefficient. Movies were composed of 100,000 frames and simulated by fixing the two emitters  $r_0/2$  apart (blue dots), where  $r_0$  is the Airy disk radius of the PSF for incoherent imaging.

being proportional to the projection on one of the sphere's axes. Under this assumption, one can

derive the  $n$ th moment  $G_n$  for the stochastic intensity trajectory of each emitter/scatterer:

$$G_n = \frac{1}{4\pi} \int_0^{2\pi} \int_0^\pi \left( \sin^2\theta \cos^2\varphi - \frac{1}{3} \right)^n \sin\theta d\theta d\varphi = \sum_{k=0}^n \binom{n}{k} \left( -\frac{1}{3} \right)^{n-k} \frac{1}{1+2k} \quad (5)$$

$$= \left( -\frac{1}{3} \right)^n {}_2F_1 \left( \frac{1}{2}, -n; \frac{3}{2}; 3 \right),$$

where  ${}_2F_1$  is the hypergeometric function. The corresponding cumulants can be calculated using the recursive formula described in Ref. [47], and are shown in Fig. 2. One notes the zero-crossing of the cumulant value at the 6th-order, resulting in SOFI images that do not display two resolved spots corresponding to the two point sources, as demonstrated for the case of incoherent imaging (Fig. 1(i)) and interference imaging with strong reference field (Fig. 1(iv)).

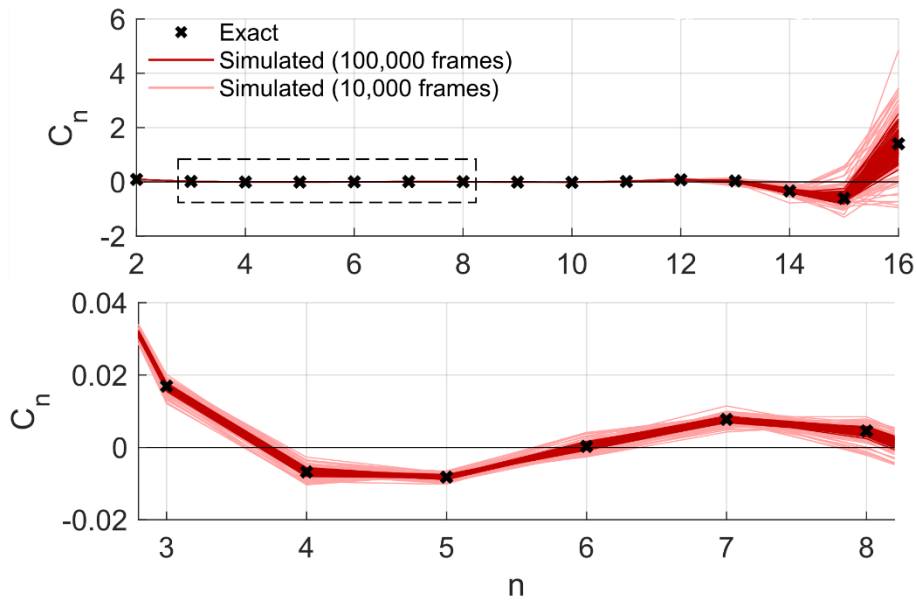


**Fig. 2.** High-order cumulant analysis of rotationally diffusing emitters/scatterers. Simulated intensity trajectories of rotating scatterers were produced by assuming an isotropic random walk on a sphere. In order to emulate the anisotropic scattering of a nanorod with one main scattering axis, the intensity at each time point of the random walk was defined as the projection of the position on the sphere onto one of its axes. Auto-cumulants  $C_n(\tau = 0)$  values of simulated trajectories were calculated up to the 16th-order (top panel), assuming a trajectory composed of 100,000 (red) and 10,000 (light red) time points. The bottom panel shows a zoomed-in view of the orders marked by a dashed square. The theoretical cumulant values, calculated using Eq. (5), are shown for each order (black cross). Due to the zero-crossing of the cumulant value at the 6th-order, the SOFI algorithm does not resolve the two point emitters in the 6th-order SOFI image in Figs. 1(i) and 1(iv).

Cases in which the cumulant value approaches zero are particularly susceptible to cusp artifacts [48], occurring whenever two neighboring emitters/scatterers form cumulants of opposite signs. As shown in Fig. 2, the more statistically limited the trajectory duration used to calculate each cumulant, the greater the distribution of its values for a given diffusion process. For a wide enough cumulant value distribution, and to a greater extent in cases where the theoretical cumulant value approaches zero, the cumulant of two temporally fluctuating emitters/scatterers can be of opposite sign, even when created by identical diffusion processes. Fig. S4 shows an example of

SOFI analysis of the interference-based movie simulated in Fig. 1, where only 10% of the movie duration is processed. One notes that the resulting SOFI images of different orders are highly variable between the various portions of the movie assumed for the analysis due to the high variability of cumulant values produced from each scatterer. This variability is caused by several factors. In the ideal case where the cumulant value from each scatterer is large compared to the cross terms, and both are of the same sign, the SOFI image results in two spots that become better resolved as the SOFI order increases. If only one of the two scatterers produces a large cumulant value, it will contribute more significantly to the corresponding SOFI image. In the case of large cumulant values of opposite signs, one observes a cusp artifact between the two scatterers. In cases where the cumulant value from each scatterer is significantly smaller compared to the cross terms, the resulting SOFI image is comprised mainly of the cross term, appearing as a spot located between the two scatterers. However, if the cumulant values from the two scatterers are comparable to the cross terms, a complex pattern emerges, where, for example, one observes three resolved spots. The SOFI images corresponding to the statistically limited movies, shown in Fig. S4, demonstrate the different cases. We note that the optimal number of frames for artifact-free SOFI also depends on the image acquisition rate. In general, the acquisition rate has to be rapid enough to capture the fluctuating optical signal from each individual particle in a manner that will produce non-negligible correlations between consecutive frames. However, temporally oversampling these intensity fluctuations will result in an unnecessarily large number of acquired frames. For the simulations described here, we sampled the rotational diffusion process with a time interval of  $\Delta t = 0.01D_r$ , where  $D_r$  is the rotational diffusion coefficient. Other fluctuative systems will require different optimal acquisition rates and total number of frames, which should be optimized for the particular underlying stochastic process in the imaged sample.

An additional important consideration that may affect coherent scattering-based imaging is the contribution of electromagnetic coupling between neighboring scatterers. It is likely that in cases where such coupling is significant, a correlation between otherwise independently fluctuating scatterers emerges. In order to assess the significance of electromagnetic coupling in practical applications, we produced simulated movies, via full wave-optical calculations [49,50], composed of images formed by two rotating neighboring dipoles, taking into account the dipole-dipole interaction. This interaction is described by the following equations:

$$\begin{aligned}\mathbf{p}_1(\mathbf{r}_1) &= \alpha_1 \hat{\mathbf{e}}_1 \{ \hat{\mathbf{e}}_1 \cdot [\mathbf{E}_{\text{exc}}(\mathbf{r}_1) + \hat{\mathbf{G}}(\mathbf{r}_1, \mathbf{r}_2) \cdot \mathbf{p}_2(\mathbf{r}_2)] \} \\ \mathbf{p}_2(\mathbf{r}_2) &= \alpha_2 \hat{\mathbf{e}}_2 \{ \hat{\mathbf{e}}_2 \cdot [\mathbf{E}_{\text{exc}}(\mathbf{r}_2) + \hat{\mathbf{G}}(\mathbf{r}_2, \mathbf{r}_1) \cdot \mathbf{p}_1(\mathbf{r}_1)] \},\end{aligned}\quad (6)$$

where  $\mathbf{p}_1(\mathbf{r}_1)$  and  $\mathbf{p}_2(\mathbf{r}_2)$  are the electric dipole moments with orientation unit vectors  $\hat{\mathbf{e}}_1 = \mathbf{p}_1/|\mathbf{p}_1|$  and  $\hat{\mathbf{e}}_2 = \mathbf{p}_2/|\mathbf{p}_2|$  that are induced in the first and second particle at positions  $\mathbf{r}_1$  and  $\mathbf{r}_2$ . Here,  $\mathbf{E}_{\text{exc}}(\mathbf{r})$  is the external exciting electric field, and  $\hat{\mathbf{G}}(\mathbf{r}_2, \mathbf{r}_1)$  is a tensor describing the electric field generated at position  $\mathbf{r}_2$  by a unit dipole at position  $\mathbf{r}_1$ . The constants  $\alpha_1$  and  $\alpha_2$  are the polarizabilities of the two particles, which generally depend on their size and shape. The solution of these coupled equations for  $\mathbf{p}_1(\mathbf{r}_1)$  and  $\mathbf{p}_2(\mathbf{r}_2)$  is given, in compact vector-matrix notation, by

$$\begin{pmatrix} \mathbf{p}_1 \\ \mathbf{p}_2 \end{pmatrix} = \begin{pmatrix} \hat{\mathbf{I}}_3 & -\alpha_1 [\hat{\mathbf{e}}_1 \otimes (\hat{\mathbf{e}}_1 \cdot \hat{\mathbf{G}}_{12})] \\ -\alpha_2 [\hat{\mathbf{e}}_2 \otimes (\hat{\mathbf{e}}_2 \cdot \hat{\mathbf{G}}_{21})] & \hat{\mathbf{I}}_3 \end{pmatrix}^{-1} \cdot \begin{pmatrix} \alpha_1 (\hat{\mathbf{e}}_1 \otimes \hat{\mathbf{e}}_1) \cdot \mathbf{E}_{\text{exc}} \\ \alpha_2 (\hat{\mathbf{e}}_2 \otimes \hat{\mathbf{e}}_2) \cdot \mathbf{E}_{\text{exc}} \end{pmatrix}, \quad (7)$$

where the six-dimensional column vector on the l.h.s has the first three components  $\mathbf{p}_1$  and the last three components  $\mathbf{p}_2$ , and the matrix on the r.h.s. is a block matrix of four  $3 \times 3$  matrices as shown, with  $\hat{\mathbf{I}}_3$  denoting a  $3 \times 3$  identity matrix, and the tensor product  $\otimes$  between two vectors defined in the usual way by  $(\mathbf{a} \otimes \mathbf{b})_{jk} = a_j b_k$ .

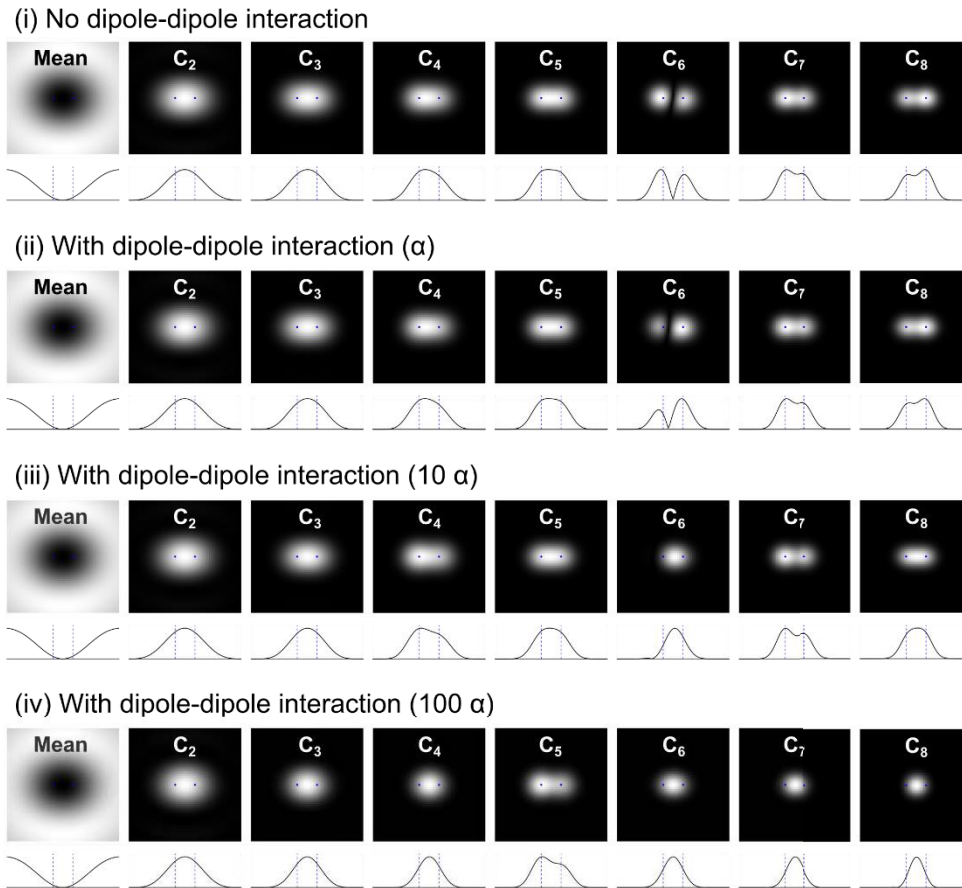


**Fig. 3.** The effect of dipole-dipole interactions on scattering-based SOFI. Simulated interference imaging movies of two neighboring rotationally diffusing dipoles were produced assuming (i) no dipole-dipole interaction, and (ii) dipole-dipole interaction calculated for point dipoles with polarizabilities associated with gold nanoparticles that are 40 nm in diameter. For each movie, the mean intensity image and auto-cumulant images ( $\tau = 0$ ) up to the 8th-order are shown (top), together with the cross-section of the line passing through both emitters (bottom). Movies composed of 100,000 frames were produced by modeling an ideal interference imaging system with a strong reference field ( $E_{ref} = 100E_{scat}$ ) operating at a wavelength of 640 nm, with the two dipoles spatially fixed 160 nm apart in a water environment above a glass substrate, generating far-field images captured via an imaging system with 100X magnification, a numerical aperture of 1.2 and an effective pixel size of 13.5 nm. The rotational diffusion trajectory of each dipole was taken to be identical to the one used for generating the movies shown in Fig. 1. In order to accentuate the effect of dipole-dipole interactions, (iii) and (iv) show the resulting SOFI images calculated for movies produced by assuming polarizabilities that are 10x and 100x higher, respectively, than the one used for case (ii).

Figure 3 shows the resulting SOFI images for simulated interference imaging movies with two neighboring dipoles rotating in a manner identical to the ones assumed for Fig. 1. The two rotating dipoles were spatially fixed 160 nm apart from each other and assumed to be imaged using 640 nm light, with other imaging parameters set to produce a case comparable to the one shown in Fig. 1. Figures 3(i) and 3(ii) show the resulting SOFI images for the case without and

with dipole-dipole interaction, respectively, where the polarizabilities  $\alpha$  of both rotating dipoles in the latter case were taken to be as one calculated for gold nanoparticles 40 nm in diameter [51]. One observes that under these assumptions, the effect of electromagnetic coupling between the dipoles is negligible, apart from slight influence in the 6th SOFI order, where, as described above, the contribution of the cross-term between the two intensity trajectories of both particles is already very significant. We note that while both Fig. 1(iv) and Fig. 3(i) describe similar conditions for interference imaging of two non-interacting particles, the latter contains the added complexity of the angular dependence in the formed PSF from each dipole. Thus, one can notice slight differences between the SOFI images in Figs. 1(iv) and 3(i). These results demonstrate that dipole-dipole interaction can be likely neglected in many practical cases of scattering-based super-resolution imaging. However, for very high polarizabilities, or very close particles, such interactions will eventually lead to more significant effects that hinder super-resolution imaging. In order to demonstrate this point, we increased the polarizabilities of both particles by a factor of 10 and 100, shown in Figs. 3(iii) and 3(iv), respectively. There, one notices a greater difference from the non-interacting case shown in Fig. 3(i). In the extreme case of very high polarizabilities, as in Fig. 3(iv), dipole-dipole coupling removes the statistical independence between the stochastic scattered intensity trajectories of both particles, resulting in significant contributions from the cross-cumulant between neighboring particles. Thus, the corresponding SOFI images in Fig. 3(iv) contain only one spot located halfway between both dipoles. We note that the above electromagnetic simulations approximated both particles as point dipoles. However, particle geometry can play a significant role in image formation in cases where the particles' size is comparable with the distance between them. Finally, we show in Fig. S5 the theoretical prediction for SOFI analysis performed on incoherent and interference-based coherent imaging of one particle translocating between two neighboring positions. This example also illustrates the case of two neighboring fluctuating emitters/scatterers in a completely anti-correlated manner. Due to the statistical dependence between the two fluctuating emitters/scatterers, the cross-term between the two particles does not vanish, resulting in its significant contribution to the resulting SOFI images. For this case, the resulting SOFI images of all orders, for both the incoherent and interference-based coherent imaging modalities, show two spots centered further apart than the two translocation positions.

While the analysis in this section was focused on the essential minimal model of two neighboring particles, the considerations described here can be extended to multi-particle systems. In addition, we note that all coherent imaging modalities addressed here were assumed to be fully coherent, as the distance between the two point particles was smaller than the coherence length for practical illuminating fields. Further analysis, accounting for spatial and temporal coherence [52], as well as partial coherence [53], should be considered in the general application of sSOFI for more complex systems.

### 3.2. Experimental demonstration of scattering-based SOFI

In order to demonstrate the application of SOFI algorithms to scattering-based imaging modalities, we constructed a custom-built microscope capable of simultaneous reflection interference and epifluorescence imaging, as illustrated in Fig. S2 and further described in the 'Materials and Methods' section and Supplement 1. Scanning electron microscopy (SEM) was used to observe the nanoparticles that produced the scattered light and correlative imaging between optical and SEM microscopies was performed using an indexed chrome micro-grid fabricated on top of the glass coverslip (Fig. S3). Figure 4 shows an example of such a dual imaging modality experiment, where two individual AuNRs, as seen from the SEM image in Fig. 4(B), form a destructive interference pattern in the optical interference image in Fig. 4(A).

In a manner analogous to nanoscale calibration samples used for fluorescence-based super-resolution microscopies [43,54], we formed scattering-based nanorulers by binding AuNRs

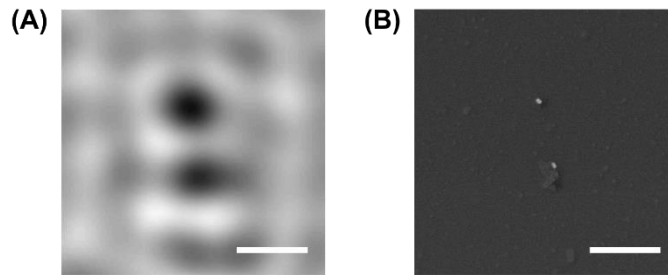


**Fig. 4.** Correlative imaging: Interference-based and SEM imaging of AuNRs. (A) Two AuNR monomers were imaged via reflection interference microscopy, each forming a destructive interference pattern. Interference microscopy was performed with a 640 nm incoming laser beam. Background correction was applied to the raw interference image as described in the ‘Materials and Methods’ section. (B) SEM image of the same region shown in (A), localized using a grid pattern fabricated on the glass coverslip. Scale bars: 500 nm.

at two defined positions on rectangular DNA origami structures. As illustrated in Fig. 5(A), the two AuNRs bind at the opposing corners of the rectangular origami structure. In addition, four fluorophores (ATTO 647N) were bound at the center of the structures, serving as a verification that the scattered light from the AuNRs is associated with a DNA origami structure. Figures 5(B) and 5(C) show AFM images of the origami structures and SEM images of the bound AuNRs, respectively. Such scattering-based nano-structures can be utilized to test and develop scattering-based super-resolution methodologies. In order to test the feasibility of sSOFI, we acquired reflectance interference movies capturing fluctuations of the scattered light created by the rotational diffusion of these bound AuNRs, which scatter light in an anisotropic manner. Figures 6(A) and 6(B) show the mean interference and SEM image, respectively, of a region containing two individual AuNRs, and one AuNR dimer. We note that the two AuNRs in the dimer seem to be in contact with one another in the SEM image (Fig. 6(B)). We observed such contact between AuNRs in the SEM images of several AuNR dimers, verified to be associated with the DNA origami structure by the colocalized fluorescence signal from the fluorophores bound to the structure. This contact between the AuNRs may have occurred due to a drying artifact during sample preparation for SEM imaging, which included an evaporation process prior to the sputtering of the conductive iridium layer. Thus, it is likely that the two AuNRs in such dimers were not in contact with each other prior to evaporation, and were able to rotationally diffuse. Since the interference imaging detection path described in this work was polarization-sensitive, the rotational diffusion of these AuNRs was translated to intensity fluctuations of the detected scattered light. We note that while we use a polarization-sensitive detection scheme in order to generate fluctuative optical signal from each particle, one could also utilize it to detect single-particle orientation, as demonstrated in Ref. [55].

In the case of the dimer shown in Fig. 6, the combined PSFs demonstrated such temporally fluctuative patterns, which lent itself to further SOFI analysis. Figure 6(C) shows the result of the SOFI analysis applied to an interference imaging movie, composed of 10,000 frames, of that sample region. We note that the number of captured frames was limited by the axial drift of the sample from the objective. For the following demonstrations, SOFI analysis was performed by calculating the auto-cumulant value of each pixel at a time lag of  $\tau = 1$  frame, as it reduces the noise on the final SOFI image caused by any noise source that has the property of having no correlation between frames [25]. Speckle background correction was performed as described in the ‘Materials and Methods’ section. However, no further image processing, such as deconvolution, was utilized for the calculation of the SOFI images. In the SOFI-analyzed images shown in Fig. 6(C), one observes two resolved spots exhibiting cusp artifacts in odd

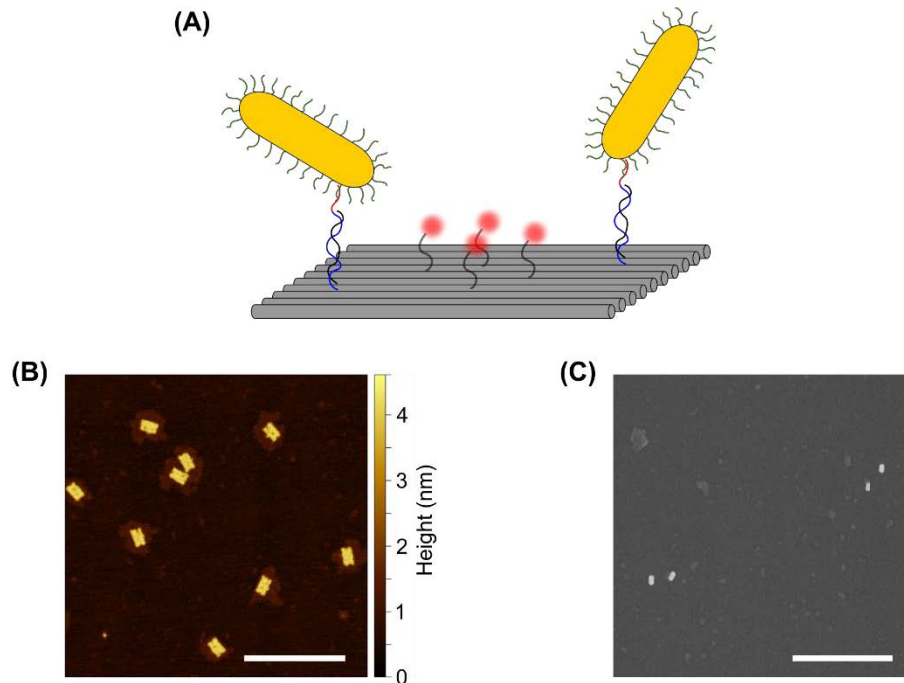


**Fig. 5.** DNA origami-based gold nanorod dimers. (A) A scheme of the rectangular origami structure used in this work, binding two gold nanorods via two DNA strands  $\sim 80$  nm apart, and four fluorophores used for colocalization between the origami structures and gold nanorods. (B) AFM image of the folded rectangular origami structures. (C) SEM image of gold nanorods bound to the origami structures, forming dimer geometries. Scale bars: 500 nm.

SOFI orders and a single spot in even SOFI orders. For comparison, Figs. 6(D) and S6(C) show the corresponding correlation function images at orders 8-13, and all orders, respectively, from which the cumulant SOFI images were calculated. In these correlation function images, one observes that the AuNR dimer primarily corresponds to a single spot in the high correlation orders. The resolvment of two spots in some SOFI orders in Fig. 6(C), and its absence in the mere correlation function images shown in Figs. 6(D) and S6(C), is the predicted outcome of the cumulant-based analysis utilized in SOFI, as it eliminates the contribution from cross-terms between neighboring particles that are present in the correlation function [25]. In other words, the emergence of two lobes in the cumulant image, and their absence in the correlation function image, demonstrates that sSOFI can detect the two neighboring scattering particles beyond the diffraction limit. However, due to cusp artifacts arising from limited statistics for the given (non-isotropic) rotational diffusion processes, or correlations between the two fluctuating scattered fields due to electrodynamic or hydrodynamic coupling between the particles, this demonstration does not resolve the exact distance between the two AuNRs. Two additional examples are shown in Fig. S7. There, two resolved spots, still exhibiting cusp artifacts, are present in even SOFI orders for the first example. The second example in Fig. S7 shows a more complicated pattern – while some SOFI orders contain two resolved spots, the orientation of the AuNR dimer is slightly different between some SOFI orders. While these examples exhibit practical complexities that emerge in SOFI analysis in general [48], the ability to calculate cumulants up to very high orders, allowed due to both the higher acquisition rates and longer acquisition durations offered by scattering-based imaging, makes these complexities even more prominent in sSOFI. In the

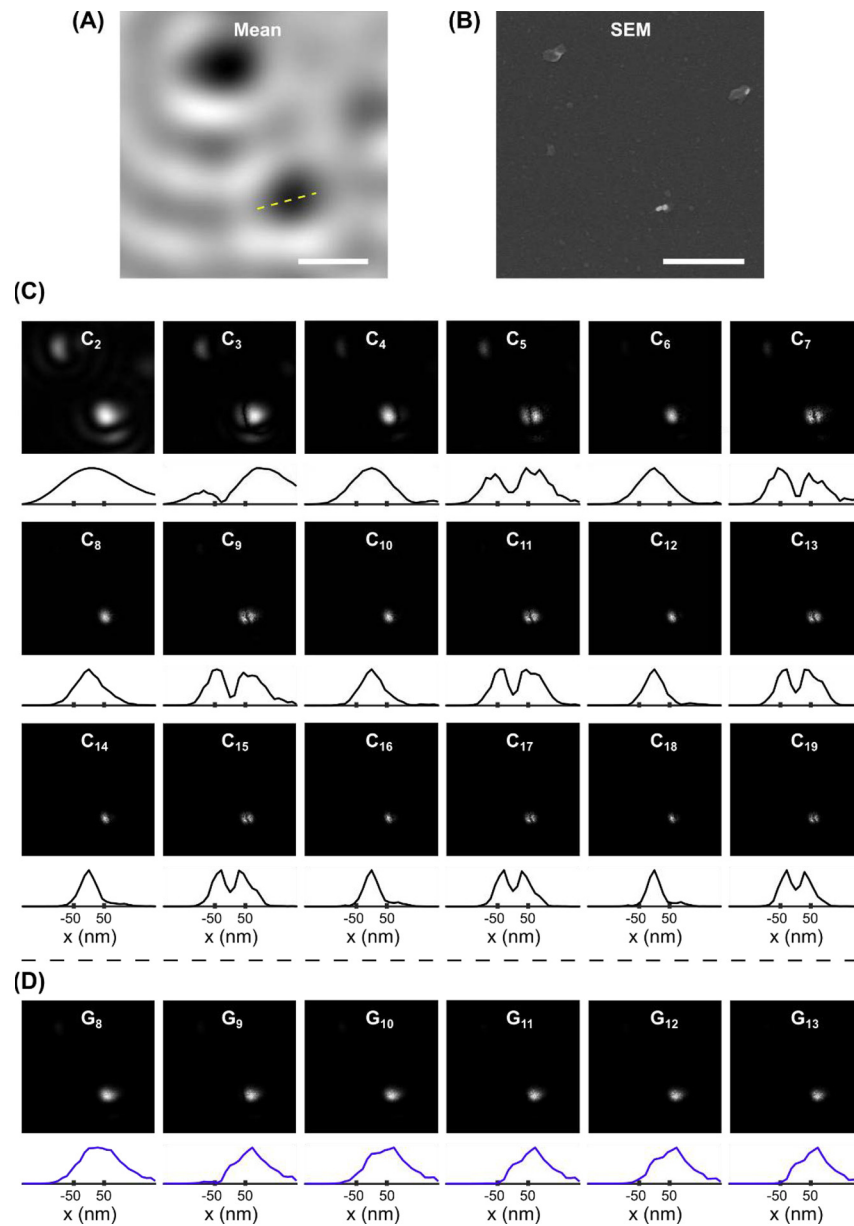


**Fig. 6.** Reflectance interference microscopy and the corresponding SOFI analysis of a gold nanorod dimer. (A) and (B) show the averaged background-corrected iSCAT image and SEM image, respectively. A movie composed of 10,000 frames was acquired (exposure time = 1 ms) using a polarized incoming beam, which results in fluctuating PSFs for the case of rotationally diffusing nanorods. Image acquisition buffer consisted of 5 mM Tris-HCl, 10 mM MgCl<sub>2</sub>, 1 mM EDTA, and 0.05% (v/v) Tween 20 (pH 8). (C) shows the SOFI auto-cumulants ( $\tau = 1$  frame) up to the 19th-order. For each order, the cross-section of the region indicated with a yellow dashed line in (A) is shown below each SOFI image. The corresponding correlation function images at orders 8-13 are shown in (D), displaying a single spot at all orders, in contrast to the two spots present in some SOFI orders. All other correlation function orders used for calculating the SOFI images in (C) are shown in Fig. S6. Scale bars: 500 nm.

experimental demonstration described above, it is evident that the rotational diffusion of the imaged AuNRs, which produces the observed intensity fluctuations, does not follow the simple isotropic rotational diffusion model described in the theoretical analysis presented in section 3-1. Moreover, asymmetric or distorted PSFs introduce further complexities, especially in high orders, where asymmetries are further distorted as the effective PSFs in the SOFI image are powers of the original PSF formed by each particle. Such highly asymmetric neighboring PSFs can form complex patterns in the final SOFI image.

Since these factors introduce challenges for achieving robust super-resolution scattering-based imaging, especially in practical applications involving complex nano-structures and cellular environments, we conclude this section by discussing experimental and computational approaches one can take in order to address these challenges. First, it may be possible to create better-controlled fluctuating scattered light signals by implementing an approach similar to points accumulation for imaging in nanoscale topography (PAINT) [56] and DNA-PAINT [43], where scatterers are allowed to transiently bind to individual sites that can be resolved via SOFI. Utilizing an approach that offers reversible binding/unbinding kinetics, as in DNA-PAINT, can allow for further control and optimization of fluctuation kinetics. Moreover, since photobleaching is not an experimental concern in scattering-based imaging, one could develop fluctuating scattering probes by utilizing the opening/closing kinetics of DNA hairpins conjugated to scattering nanoparticles. In addition, asymmetric and distorted PSFs can be accounted for by deconvolving the interference images with known PSFs captured from static nano-scatterers scanned across the imaged sample area. The images of these static nano-scatterers can be further used as training datasets for machine learning algorithms, which have already been shown to improve detection sensitivity for iSCAT microscopy [57,58]. Such approaches can enhance the capabilities of sSOFI and reduce artifacts when calculating high cumulant orders. Finally, we note that since the dimensions of the AuNRs in the above demonstration are comparable to the distance between their binding sites on the DNA origami structure, a more detailed electrodynamic study of the scattering problem, accounting for nano-plasmonic effects, is required to describe the formed image [59,60].

### 3.3. *Scattering-based SOFI as a fluctuation-based novelty filter*

In this final section, we demonstrate the application of sSOFI as an imaging processing approach for highlighting dynamic processes captured by interference imaging. The application of interference microscopy to live cell imaging is especially relevant for thin peripheral cell regions, where the number of scattering biomolecules is significant but relatively small enough to decipher unique biological dynamical structures and events such as filopodia and focal adhesions [61,62]. There, in addition to its use for super-resolution imaging, sSOFI can be utilized as a novelty filter and provide a quantitative measure for cellular activity that results in fluctuating scattering from biomolecules in a manner similar to the different variants of imaging-based correlation spectroscopy utilizing optical signals from either fluorescence emission [63,64] or scattered light [65]. Figure 7 shows the application of SOFI analysis to interference microscopy movies of membrane protrusions in live cells, allowing for a straightforward contrast enhancement of highly dynamic regions. Membrane labeling of HEK293 cells, as described in Supplement 1, was used to identify two neighboring membrane protrusions (Figs. 7(B)-(C)), which produced little contrast in both the brightfield (Fig. 7(A)) and interference images (Fig. 7(D)). However, one of the protrusions appears as a bright structure on top of a dark background in the SOFI images (Figs. 7(E)-(F)). The higher cumulant values assigned to the pixels corresponding to the active protrusion are a result of the fluctuating scattered fields either from the biomolecules diffusing and transporting within it, producing fluctuating optical signals even from isotropic scatterers, or axial movement of the protrusion itself [62]. We note that the SOFI-analyzed images display noticeable spatial oscillations, which can be either due to morphological properties of the protrusions, such as varying height from the glass surface, resulting in a periodic

interference pattern, or an imaging-related artifact due to the reflected speckle pattern. This demonstration shows that beyond its use for super-resolution imaging, sSOFI can be utilized as an activity-sensitive contrast mechanism that can be applied simultaneously with conventional fluorescence imaging with labeled biomolecules, using the same excitation light for both imaging modalities, providing information on the overall activity of biomolecules in the local environment without additional labeling. We note that while sSOFI allows for a computationally efficient and assumption-free method for highlighting dynamic regions within the cell, further analysis, such as time-differential iSCAT [66], can be applied for detecting and localizing scattering nano-objects with distinguishable transport dynamics.

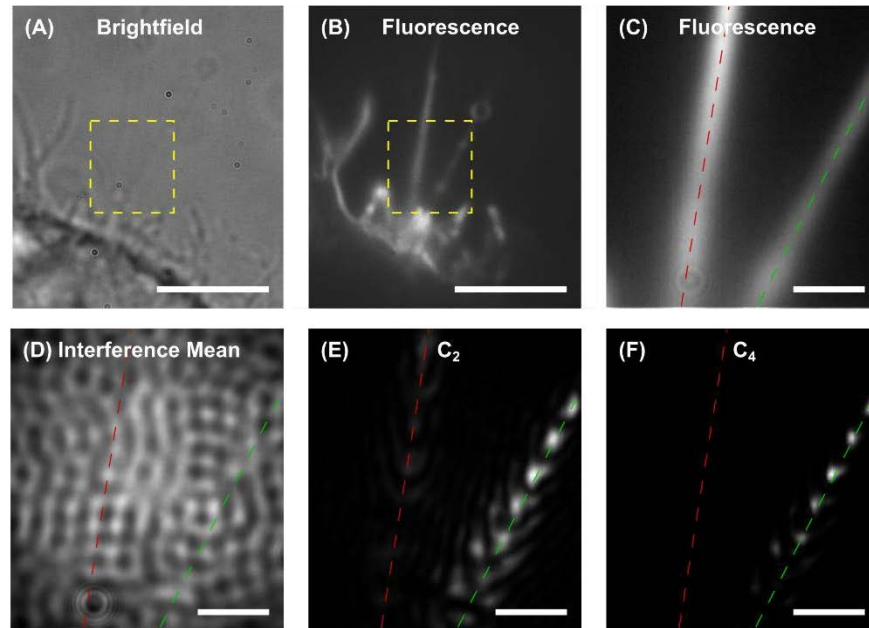


**Fig. 7.** Scattering-based SOFI analysis of membrane protrusions exhibiting fluctuative scattering. Fluorescently labeled membrane protrusions of a HEK293 cell were imaged using (A) brightfield, (B-C) fluorescence, and (D) interference microscopies. The dashed yellow squares in (A) and (B) indicate the zoomed-in regions shown in (C-F). The cell membrane, including its membrane protrusions, was labeled with Di-8-ANEPPS. For interference imaging, a movie composed of 1000 frames was acquired (exposure time = 1 ms) using a 470 nm incoming laser beam. Cellular activity that generated fluctuating scattering signals was then highlighted by SOFI analysis. The dashed green and red lines indicate the active and inactive protrusions, respectively. (E) and (F) show the 2nd and 4th-order SOFI auto-cumulant images ( $\tau = 1$  frame), respectively, for the raw interference imaging movie. Scale bars: (A-B): 5  $\mu\text{m}$ , (C-F): 1  $\mu\text{m}$ .

#### 4. Conclusion

In summary, we investigated the application of SOFI algorithms to coherent scattering-based imaging modalities. We showed that while dark-field-based imaging modalities cannot be super-resolved via SOFI algorithms due to a cross-term between the two scatterers appearing in the image formed at the camera plane, interference-based imaging modalities are suited for further super-resolution processing via SOFI algorithms. In addition, we analyzed the contribution of dipole-dipole interaction between scatterers on the formed image, and demonstrated that this interaction can be neglected in many practical cases. Since SOFI algorithms are based

on uncorrelated fluctuating signals from neighboring emitters, a mechanism for creating such fluctuations is essential for achieving super-resolved scattering-based images. While fluorescence blinking provides a source of signal fluctuations for incoherent, fluorescence-based SOFI, scattering-based imaging requires an alternative mechanism. Here, we utilized the rotational diffusion of anisotropic nanoparticles that, when imaged in a polarization-sensitive modality, can provide a source of fluctuating scattered field from each nanoparticle. In order to demonstrate the application of SOFI for achieving super-resolved images from interference-based movies, we formed AuNRs dimers by tethering them to DNA origami constructs. Such engineered scattering nano-rulers can provide a platform for the further development of scattering-based super-resolution approaches. Finally, by interference imaging membrane protrusions, we demonstrated the use of sSOFI as a novelty filter that can be utilized in order to highlight dynamic processes that produce fluctuating scattering fields. This label-free contrast-generating image processing approach could be applied to visualize dynamic events and processes captured by scattering-based imaging.

The development of scattering-based super-resolution techniques can allow one to probe biological systems without the disadvantages of fluorescence imaging, which are inherently limited due to a finite photon budget. Practically, the development of sSOFI will require one to either optimize sample preparation in order to produce reliable fluctuative scattering, by, for example, optimizing the rotational diffusion or the binding and unbinding kinetics of scattering nanoparticles, or rely on dynamic cellular processes such as diffusion and transport of small organelles or large macromolecules. Once achieved, such bleaching-free acquisition will allow for super-resolution imaging at an unprecedented temporal resolution and imaging duration.

**Funding.** HORIZON EUROPE European Research Council (669941); Israel Science Foundation (813/19); National Science Foundation (DMR-1548924).

**Acknowledgements.** We would like to thank David Bensimon for the insightful discussions.

**Disclosures.** The authors declare no conflicts of interest.

**Data availability.** All acquired and simulated movies used for the results presented in this work are available at [67]. Home-written code (MATLAB) for the analysis shown in this work is available upon request.

**Supplemental document.** See [Supplement 1](#) for supporting content.

## References

1. S.W. Hell and J. Wichmann, "Breaking the diffraction resolution limit by stimulated emission: stimulated-emission-depletion fluorescence microscopy," *Opt. Lett.* **19**(11), 780–782 (1994).
2. E. Betzig, G. H. Patterson, R. Sougrat, *et al.*, "Imaging intracellular fluorescent proteins at nanometer resolution," *Science* **313**(5793), 1642–1645 (2006).
3. M.J. Rust, M. Bates, and X.W. Zhuang, "Sub-diffraction-limit imaging by stochastic optical reconstruction microscopy (STORM)," *Nat. Methods* **3**(10), 793–796 (2006).
4. M.G.L. Gustafsson, "Surpassing the lateral resolution limit by a factor of two using structured illumination microscopy," *J. Microsc.* **198**(2), 82–87 (2000).
5. R. Schmidt, T. Weihs, C. A. Wurm, *et al.*, "MINFLUX nanometer-scale 3D imaging and microsecond-range tracking on a common fluorescence microscope," *Nat. Commun.* **12**(1), 1478 (2021).
6. K. Xu, G. Zhong, and X. Zhuang, "Actin, Spectrin, and Associated Proteins Form a Periodic Cytoskeletal Structure in Axons," *Science* **339**(6118), 452–456 (2013).
7. S. Köhler, M.W. Wojcik, K. Xu, *et al.*, "Superresolution microscopy reveals the three-dimensional organization of meiotic chromosome axes in intact *Caenorhabditis elegans* tissue," *Proc. Natl. Acad. Sci. U. S. A.* **114**(24), E4734 (2017).
8. A.N. Boettiger, B. Bintu, J. R. Moffitt, *et al.*, "Super-resolution imaging reveals distinct chromatin folding for different epigenetic states," *Nature* **529**(7586), 418–422 (2016).
9. I. Braslavsky, R. Amit, B. M. Jaffar Ali, *et al.*, "Objective-type dark-field illumination for scattering from microbeads," *Appl. Opt.* **40**(31), 5650–5657 (2001).
10. G. Wiegand, K.R. Neumaier, and E. Sackmann, "Microinterferometry: three-dimensional reconstruction of surface microtopography for thin-film and wetting studies by reflection interference contrast microscopy (RICM)," *Appl. Opt.* **37**(29), 6892–6905 (1998).
11. K. Lindfors, T. Kalkbrenner, P. Stoller, *et al.*, "Detection and Spectroscopy of Gold Nanoparticles Using Supercontinuum White Light Confocal Microscopy," *Phys. Rev. Lett.* **93**(3), 037401 (2004).

12. S. Spindler, J. Ehrig, K. König, *et al.*, “Visualization of lipids and proteins at high spatial and temporal resolution via interferometric scattering (iSCAT) microscopy,” *J. Phys. D: Appl. Phys.* **49**(27), 274002 (2016).
13. J. Andrecka, J. Ortega Arroyo, K. Lewis, *et al.*, “Label-free Imaging of Microtubules with Sub-nm Precision Using Interferometric Scattering Microscopy,” *Biophys. J.* **110**(1), 214–217 (2016).
14. L.S. Mosby, N. Hundt, G. Young, *et al.*, “Myosin II Filament Dynamics in Actin Networks Revealed with Interferometric Scattering Microscopy,” *Biophys. J.* **118**(8), 1946–1957 (2020).
15. S. Inoué and R. Oldenbourg, “Microtubule Dynamics in Mitotic Spindle Displayed by Polarized Light Microscopy,” *Mol. Biol. Cell* **9**(7), 1603–1607 (1998).
16. M. Mahamdeh, S. Simmert, A. Luchniak, *et al.*, “Label-free high-speed wide-field imaging of single microtubules using interference reflection microscopy,” *J. Microsc.* **272**(1), 60–66 (2018).
17. Y. Mao, L. Han, and Z. Yin, “Cell mitosis event analysis in phase contrast microscopy images using deep learning,” *Med. Image Anal.* **57**, 32–43 (2019).
18. J. Kang, L. Lim, Y. Lu, *et al.*, “A unified mechanism for LLPS of ALS/FTLD-causing FUS as well as its modulation by ATP and oligonucleic acids,” *PLoS Biol.* **17**(6), e3000327 (2019).
19. J. Reed, J. Chun, T. A. Zangle, *et al.*, “Rapid, Massively Parallel Single-Cell Drug Response Measurements via Live Cell Interferometry,” *Biophys. J.* **101**(5), 1025–1031 (2011).
20. G. Young, N. Hundt, D. Cole, *et al.*, “Quantitative mass imaging of single biological macromolecules,” *Science* **360**(6387), 423–427 (2018).
21. T. Ling, K. C. Boyle, V. Zuckerman, *et al.*, “High-speed interferometric imaging reveals dynamics of neuronal deformation during the action potential,” *Proc. Natl. Acad. Sci.* **117**(19), 10278–10285 (2020).
22. Y. Park, C. Depeursinge, and G. Popescu, “Quantitative phase imaging in biomedicine,” *Nat. Photonics* **12**(10), 578–589 (2018).
23. B. Bhaduri, C. Edwards, H. Pham, *et al.*, “Diffraction phase microscopy: principles and applications in materials and life sciences,” *Adv. Opt. Photonics* **6**(1), 57–119 (2014).
24. V.N. Astratov, Y. B. Sahel, Y. C. Eldar, *et al.*, “Roadmap on Label-Free Super-Resolution Imaging,” *Laser Photonics Rev.* **17**(12), 202200029 (2023).
25. T. Dertinger, R. Colyer, G. Iyer, *et al.*, “Fast, background-free, 3D super-resolution optical fluctuation imaging (SOFI),” *Proc. Natl. Acad. Sci.* **106**(52), 22287–22292 (2009).
26. S. Geissbuehler, N. L. Bocchio, C. Dellagiacomia, *et al.*, “Mapping molecular statistics with balanced super-resolution optical fluctuation imaging (bSOFI),” *Opt. Nano.* **1**, 4 (2012).
27. T. Dertinger, R. Colyer, R. Vogel, *et al.*, “Achieving increased resolution and more pixels with Superresolution Optical Fluctuation Imaging (SOFI),” *Opt. Express* **18**(18), 18875–18885 (2010).
28. S. Stallinga, N. Radmacher, A. Delon, *et al.*, “Optimal transfer functions for bandwidth-limited imaging,” *Phys. Rev. Res.* **4**(2), 023003 (2022).
29. X. Zhang, X. Chen, Z. Zeng, *et al.*, “Development of a reversibly switchable fluorescent protein for super-resolution optical fluctuation imaging (SOFI),” *ACS Nano* **9**(3), 2659–2667 (2015).
30. T. Dertinger, M. Heilemann, R. Vogel, *et al.*, “Superresolution Optical Fluctuation Imaging with Organic Dyes,” *Angew. Chem., Int. Ed.* **49**(49), 9441–9443 (2010).
31. A.M. Chizhik, S. Stein, M. O. Dekaliuk, *et al.*, “Super-Resolution Optical Fluctuation Bio-Imaging with Dual-Color Carbon Nanodots,” *Nano Lett.* **16**(1), 237–242 (2016).
32. L. Kiskeya, R. Brunetti, L. J. Tauzin, *et al.*, “Characterization of Porous Materials by Fluorescence Correlation Spectroscopy Super-resolution Optical Fluctuation Imaging,” *ACS Nano* **9**(9), 9158–9166 (2015).
33. S. Cho, J. Jang, C. Song, *et al.*, “Simple super-resolution live-cell imaging based on diffusion-assisted Förster resonance energy transfer,” *Sci. Rep.* **3**(1), 1208 (2013).
34. M. Kim, C. Park, C. Rodriguez, *et al.*, “Superresolution imaging with optical fluctuation using speckle patterns illumination,” *Sci. Rep.* **5**(1), 16525 (2015).
35. T. Dertinger, J. Xu, O. Naini, *et al.*, “SOFI-based 3D superresolution sectioning with a widefield microscope,” *Opt. Nanoscopy* **1**(1), 2 (2012).
36. S. Geissbuehler, A. Sharipov, A. Godinat, *et al.*, “Live-cell multiplane three-dimensional super-resolution optical fluctuation imaging,” *Nat. Commun.* **5**(1), 5830 (2014).
37. X. Chen, Z. Zeng, H. Wang, *et al.*, “Three-dimensional multimodal sub-diffraction imaging with spinning-disk confocal microscopy using blinking/fluctuating probes,” *Nano Res.* **8**(7), 2251–2260 (2015).
38. X. Chen, W. Zong, R. Li, *et al.*, “Two-photon light-sheet nanoscopy by fluorescence fluctuation correlation analysis,” *Nanoscale* **8**(19), 9982–9987 (2016).
39. T. Chaigne, B. Arnal, S. Vilov, *et al.*, “Super-resolution photoacoustic imaging via flow-induced absorption fluctuations,” *Optica* **4**(11), 1397–1404 (2017).
40. T. Dertinger, A. Pallaoro, G. Braun, *et al.*, “Advances in superresolution optical fluctuation imaging (SOFI),” *Q. Rev. Biophys.* **46**(2), 210–221 (2013).
41. G. González-Rubio, V. Kumar, P. Llombart, *et al.*, “Disconnecting Symmetry Breaking from Seeded Growth for the Reproducible Synthesis of High Quality Gold Nanorods,” *ACS Nano* **13**(4), 4424–4435 (2019).
42. B. Liu and J. Liu, “Freezing Directed Construction of Bio/Nano Interfaces: Reagentless Conjugation, Denser Spherical Nucleic Acids, and Better Nanoflakes,” *J. Am. Chem. Soc.* **139**(28), 9471–9474 (2017).

43. J. Schnitzbauer, M. T. Strauss, T. Schlichthaerle, *et al.*, “Super-resolution microscopy with DNA-PAINT,” *Nat. Protoc.* **12**(6), 1198–1228 (2017).
44. D. Nečas and P. Klapetek, “Gwyddion: an open-source software for SPM data analysis,” *Cent. Eur. J. Phys.* **10**(1), 181–188 (2012).
45. J. Ortega Arroyo, D. Cole, and P. Kukura, “Interferometric scattering microscopy and its combination with single-molecule fluorescence imaging,” *Nat. Protoc.* **11**(4), 617–633 (2016).
46. A. Novikov, D. Kuzmin, and O. Ahmadi, “Random walk methods for Monte Carlo simulations of Brownian diffusion on a sphere,” *Applied Mathematics and Computation* **364**, 124670 (2020).
47. J.M. Mendel, “Tutorial on higher-order statistics (spectra) in signal processing and system theory: theoretical results and some applications,” *Proc. IEEE* **79**(3), 278–305 (1991).
48. X. Yi and S. Weiss, “Cusp-artifacts in high order superresolution optical fluctuation imaging,” *Biomed. Opt. Express* **11**(2), 554–570 (2020).
49. M. Böhmer and J. Enderlein, “Orientation imaging of single molecules by wide-field epifluorescence microscopy,” *J. Opt. Soc. Am. B* **20**(3), 554–559 (2003).
50. M. Fazel, K. S. Grussmayer, B. Ferdman, *et al.*, “Fluorescence microscopy: A statistics-optics perspective,” *Rev. Mod. Phys.* **96**(2), 025003 (2024).
51. L. Novotny and B. Hecht, *Principles of Nano-Optics*. 2 ed. (Cambridge University Press, 2012).
52. W. Singer, M. Totzeck, and H. Gross, *Handbook of Optical Systems*, Volume 2: Physical Image Formation (Wiley, 2006).
53. C.J.R. Sheppard, “Defocused transfer function for a partially coherent microscope and application to phase retrieval,” *J. Opt. Soc. Am. A* **21**(5), 828–831 (2004).
54. M. Raab, I. Jusuk, J. Molle, *et al.*, “Using DNA origami nanorulers as traceable distance measurement standards and nanoscopic benchmark structures,” *Sci. Rep.* **8**(1), 1780 (2018).
55. I.-B. Lee, H.-M. Moon, J.-H. Joo, *et al.*, “Interferometric scattering microscopy with polarization-selective dual detection scheme: capturing the orientational information of anisotropic nanometric objects,” *ACS Photonics* **5**(3), 797–804 (2018).
56. A. Sharonov and R.M. Hochstrasser, “Wide-field subdiffraction imaging by accumulated binding of diffusing probes,” *Proc. Natl. Acad. Sci.* **103**(50), 18911–18916 (2006).
57. M. Dahmardeh, H. Mirzaalian Dastjerdi, H. Mazal, *et al.*, “Self-supervised machine learning pushes the sensitivity limit in label-free detection of single proteins below 10 kDa,” *Nat. Methods* **20**(3), 442–447 (2023).
58. M.J. Boyle, Y.E. Goldman, and R.J. Composto, “Enhancing Nanoparticle Detection in Interferometric Scattering (iSCAT) Microscopy Using a Mask R-CNN,” *J. Phys. Chem. B* **127**(16), 3737–3745 (2023).
59. M.R. Shcherbakov, A. T. Le, N. Dubrovina, *et al.*, “Plasmon ruler with gold nanorod dimers: utilizing the second-order resonance,” *Opt. Lett.* **40**(7), 1571–1574 (2015).
60. Z. Chen, X. Lan, Yu-Che Chiu, *et al.*, “Strong Chiroptical Activities in Gold Nanorod Dimers Assembled Using DNA Origami Templates,” *ACS Photonics* **2**(3), 392–397 (2015).
61. J.-S. Park, I.-B. Lee, H.-M. Moon, *et al.*, “Label-free and live cell imaging by interferometric scattering microscopy,” *Chem. Sci.* **9**(10), 2690–2697 (2018).
62. J.-S. Park, I.-B. Lee, H.-M. Moon, *et al.*, “Fluorescence-Combined Interferometric Scattering Imaging Reveals Nanoscale Dynamic Events of Single Nascent Adhesions in Living Cells,” *J. Phys. Chem. Lett.* **11**(23), 10233–10241 (2020).
63. N.O. Petersen, P.L. Höddelius, P.W. Wiseman, *et al.*, “Quantitation of membrane receptor distributions by image correlation spectroscopy: concept and application,” *Biophys J.* **65**(3), 1135–1146 (1993).
64. J.W. Krieger, A. P. Singh, N. Bag, *et al.*, “Imaging fluorescence (cross-) correlation spectroscopy in live cells and organisms,” *Nat. Protoc.* **10**(12), 1948–1974 (2015).
65. Y.-T. Hsiao, I.-H. Liao, B.-K. Wu, *et al.*, “Probing chromatin condensation dynamics in live cells using interferometric scattering correlation spectroscopy,” *Commun. Biol.* **7**(1), 763 (2024).
66. J.-S. Park, Il-Buem Lee, H.-M. Moon, *et al.*, “Long-term cargo tracking reveals intricate trafficking through active cytoskeletal networks in the crowded cellular environment,” *Nat. Commun.* **14**(1), 7160 (2023).
67. S. Yudovich, G. Posnjak, L. Shani, *et al.*, “Scattering-based super-resolution optical fluctuation imaging,” Zenodo (2025). <https://doi.org/10.5281/zenodo.12612205>